Article ID: 1006-8775(2024)01-0061-15

# Mesoscale and Microphysical Characteristics of a Double Rain Belt Event in South China on May 10–13, 2022

GUO Zhao-hua (郭照华)[1], CHEN Yun (谌　芸)[2,1,3], XIAO Tian-gui (肖天贵)[1], ZENG Zhi-lin (曾智琳)[4]

(1. School of Atmospheric Sciences, Chengdu University of Information Technology, Chengdu 610225 China; 2. National Meteorological Center, Beijing 100081 China; 3. Southern Marine Science and Engineering Guangdong Laboratory (Zhuhai), Zhuhai, Guangdong 519082 China; 4. Guangdong Meteorological Observatory, Guangzhou 510640 China)

**Abstract:** A second rain belt sometimes occurs ahead of a frontal rain belt in the warm sector over coastal South China, leading to heavy precipitation. We examined the differences in the mesoscale characteristics and microphysics of the frontal and warm sector rain belts that occurred in South China on May 10–13, 2022. The southern rain belt occurred in an environment with favorable mesoscale conditions but weak large-scale forcing. In contrast, the northern rain belt was related to low-level horizontal shear and the surface-level front. The interaction between the enhanced southeasterly winds and the rainfall-induced cold pool promoted the persistent growth of convection along the southern rain belt. The convective cell propagated east over the coastal area, where there was a large temperature gradient. The bow-shaped echo in this region may be closely related to the rear-inflow jet. By contrast, the initial convection of the northern rain belt was triggered along the front and the region of low-level horizontal shear, with mesoscale interactions between the enhanced warm-moist southeasterly airflow and the cold dome associated with the earlier rain. The terrain blocked the movement of the cold pool, resulting in the stagnation of the frontal convective cell at an early stage. Subsequently, a meso-$\gamma$-scale vortex formed during the rapid movement of the convective cell, corresponding to an enhancement of precipitation. The representative raindrop spectra for the southern rain belt were characterized by a greater number and higher density of raindrops than the northern rain belt, even though both resulted in comparable hourly rainfalls. These results help us better understand the characteristics of double rain belts over South China.

**Key words:** double rain belts in South China; mesoscale rainstorm; cyclonic shear line; cold pool; bow-shaped echo; microphysical characteristics

**CLC number:** P426.62 **Document code:** A

**Citation:** GUO Zhao-hua, CHEN Yun, XIAO Tian-gui, et al. Mesoscale and Microphysical Characteristics of a Double Rain Belt Event in South China on May 10–13, 2022 [J]. Journal of Tropical Meteorology, 2024, 30(1): 61-75, https://doi.org/10.3724/j.1006-8775.2024.007

## 1 INTRODUCTION

The phenomenon of "double rain belts"–that is, a frontal rain belt and a warm convective rain belt occurring at the same time–can be seen in long-term operational weather forecasts (Lin et al. [1]), although the manifestation and mechanism of formation of the two rain belts are different (Lin et al. [2]; Zhang et al. [3]). These events can lead to heavy or extreme hourly rainfall, and the risk of disaster is extremely high (Hallegatte et al. [4]). These frontal rain belts occur in the Yangtze River Basin or northern South China, where the occurrence frequency of the southern rain belt in South China is >40 % (Ding et al. [5]). In-depth analyses focused on Jianghuai and South China indicate that double rain belts often occur in South China after the onset of the South China Sea monsoon (Ding et al. [6,7]; Liu et al. [8]; Wang et al. [9]; Du [10]; Luo et al. [11]; Yang et al. [12]; Yan et al. [13]). There are clear differences in the activities of mesoscale cloud and rain clusters, the dynamic structure of convective systems, the mechanism of atmospheric instability, water vapor transport, and the mesoscale environmental conditions, which may be why it is difficult to predict heavy rain in the warm sector (Zhao et al. [14]; Wang [15]).

A large number of studies have shown that the occurrence time and location of rainstorms are closely related to the convection initiation mechanism. The intrusion of boundary layer cold air into South China is the main mechanism initiating rainstorms but is often ignored in operational forecasts (Zhao and Zhou [16]; Menard and Fritsch [17]). The terrain in South China is both complex and diverse (Huang et al. [18]; Bao [19]) and the synergistic forcing of warm-wet air and the local mesoscale terrain can induce a surface mesoscale convergence line, a mesoscale vortex and other systems, leading to a significant increase in precipitation (Xia and Zhao [20]; Miao et al. [21]; Li et al. [22]; Wang et al. [23]). Statistical studies have shown that heavy rainfall in South China is generally caused by multiple successive mesoscale convective systems (Kong and Lin [24]; Meng

**Received** 2023-03-24; **Revised** 2023-11-15; **Accepted** 2024-02-15

**Funding:** National Natural Science Foundation of China (41930972, 52239006, 41975001)

**Biography:** GUO Zhao-hua, postgraduate student, primarily undertaking research on mesoscale meteorology.

**Corresponding author:** CHEN Yun, e-mail: chenyun@cma.gov.cn

et al. [25]; Zhang et al. [26]) and the radar echo backward propagation and train effect clearly affect the duration of heavy rainstorms (Sun et al. [27]; Yang et al. [28]). However, how microphysical processes directly affect rainfall intensity and the microphysical characteristics of different precipitation processes are still unclear. Heavy raindrops during convective precipitation in spring affect the intensity of rainfall in northern Guangdong (He et al. [29]). The raindrop spectra of extreme rainfall in the warm sector of western Guangdong are characterized by warm precipitation, and the number concentration of small raindrops is much higher than the summer average for South China. The participation of large raindrops leads to an improvement in the efficiency and intensity of precipitation (Ye et al. [30]). Some studies have also found that the convective intensity of the heavy rainfall in the coastal warm sector of South China is stronger, the raindrop size is larger, and the liquid water content is higher than in frontal rainfall in northern South China (Han et al. [31]). There are still difficulties in forecasting mesoscale rainstorms in the frontal rain belt. The intensity of warm sector precipitation is stronger than that of frontal precipitation, but the prediction ability of mainstream numerical models and forecasters is still limited (Chen et al. [32]; Wu et al. [33]; Wu and Luo [34]; He et al. [35]). The differences in the microphysical characteristics of double rain belts are unclear due to the limited microphysical observations available for precipitation in South China, and further studies are therefore required.

A double rain belt event occurred in South China on May 10–13, 2022, with significant mesoscale rainstorm centers in both rain belts. We review the background atmospheric circulation and characteristics of precipitation, focusing on the mesoscale evolution of the rainstorm centers and the differences in convective structure and microphysical characteristics of local extreme rainfall. This work deepens our scientific understanding of double rain belts and provides support for improving the accuracy of their prediction.

## 2 DATA AND METHOD

In this study, ERA5 reanalysis data at a horizontal spatial resolution of 0.25°×0.25° and a time resolution of one hour from the European Centre for Medium-Range Weather Forecasts (ECMWF) was used to analyze the background atmospheric circulation. Surface observational data, the bright body temperature (TBB) products from the FY2G satellite, Guangzhou dual-polarization radar, and raindrop spectrometers in Zhuhai and Fogang were used to perform mesoscale and microphysical characteristics.

## 3 BACKGROUND CIRCULATION AND REVIEW OF THE EVENT

### 3.1 *Background atmospheric circulation*

Figure 1 shows that, during this event, South China was located in a fan-shaped divergence area on the eastern side of the South Asian High. The upper levels along the coast were transported by a strong northwesterly divergent air current. The upper trough moved east to the eastern coast of China at 500 hPa, and South China was at the base of the upper trough. The short wavelength trough continued to move east, and the fluctuation glided to the

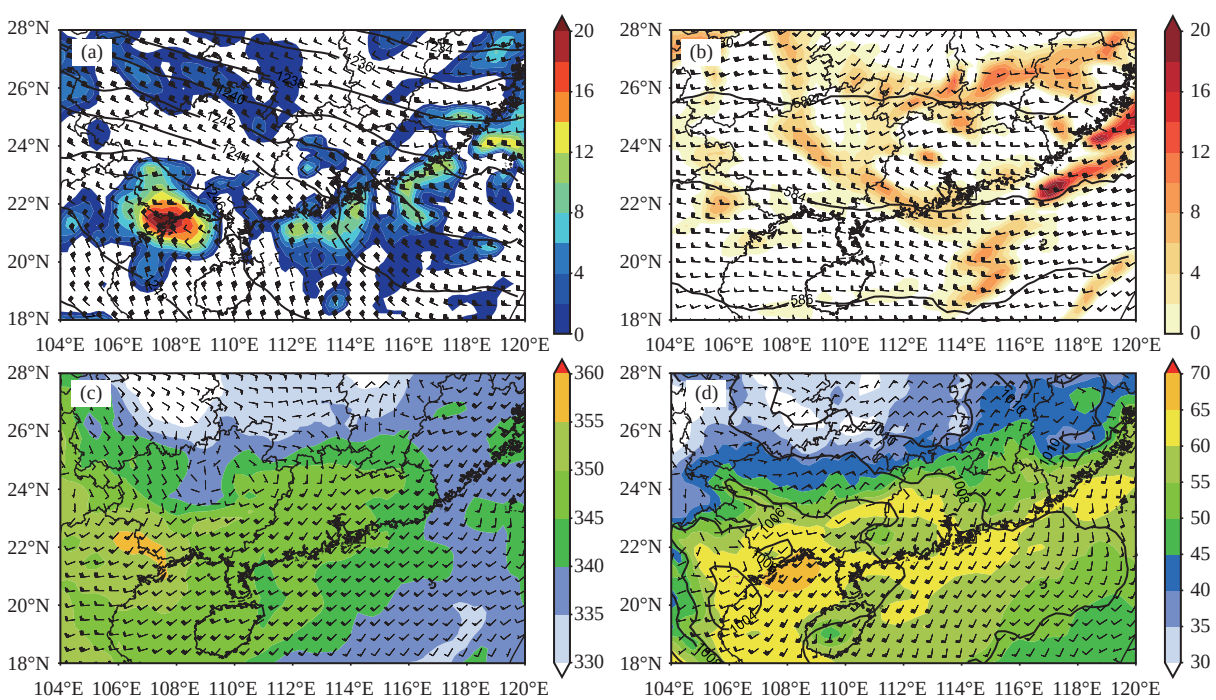


**Figure 1**. (a) Geopotential height (contour lines, units: dagpm), wind and divergence (color shading, units: $\times 10^{-5} s^{-1}$) at 200 hPa. (b) Geopotential height (contour lines, units: dagpm), wind and vorticity at 500 hPa (color shading, units: $\times 10^{-5} s^{-1}$). (c) Wind and pseudo-equivalent potential temperature at 850 hPa (color shading, units: K). (d) Wind at 925 hPa, sea level pressure (contour lines, units: hPa), and precipitable water (PWAT, color shading, units: mm) at 05:00 BJT May 11, 2022.

west of the Zhujiang River estuary. The low-level shear line and front moved south to northern South China, with the front controlled by a southwesterly air current. The low-level jet structure was established, and the vortex formed and developed at 850 and 925 hPa. The south of the front was a significant low-trough area located in the high-energy zone with a pseudo-equivalent potential temperature ($\theta_{se}$) ⩾345 K). The amount of atmospheric precipitable water in the coastal area was >60 mm. The extremely unstable atmospheric stratification and the water vapor transport conditions in South China favored the occurrence of rainstorms and convective rainfall.

3.2 *Analysis of precipitation characteristics*

Figure 2a shows that heavy rainfall occurred in South China, and some areas experienced torrential rain. Two belts of torrential rain were formed 200–300 km apart in the coastal area of Guangdong and northern South China. One rain belt was located between Yangjiang and Shanwei (the southern rain belt, D2) and was roughly parallel to the coastline. The mesoscale rainstorm center of rain belt D2 was located on the western coast of the Zhujiang river estuary, and heavy rainfall (⩾250 mm) was observed at 79 (6.2%) of the automatic stations in Guangdong. The other rain belt was located from Qingyuan to the northern part of Huizhou (the northern rain belt, D1), with a northwest-southeast orientation. The mesoscale rainstorm center was situated in Fogang, where 30 (2.4%) automatic stations recorded torrential rain. The heavy rainstorm (between the double rain belts) in the north of Yangjiang was caused by the southward movement of the frontal system.

We selected the European Centre for Medium-Range Weather Forecasts (ECMWF) and the China Meteorological Administration CMA-GFS and CMA-GD models (Fig. 2b-d) commonly used in operational forecasts. The CMA-GD model forecast reflected the shape and intensity of the double rain belt, but there was still an error in the actual area of precipitation. The ECMWF model was more effective in predicting the northern rain belt than the coastal rain belt. However, there was a significant difference from the actual situation. The CMA-GFS model was unable to describe the characteristics of the double rain belts. This analysis shows that the prediction was unsatisfactory, indicating the need to study double rain belts.

The representative stations for the double rain belts showed clear characteristics at each stage of the events (Fig. 3). The maximum cumulative rainfall of the southern rain belt was 724.7 mm in Sanxiang. The heavy rainfall started slightly later here but lasted for a longer time. The night-time characteristics of the heavy rainfall were significant, with clear stages and some volatility. The rainfall can be divided into two stages: 00:00–12:00 on May 11 and 05:00–21:00 on May 12, and the short period of heavy precipitation ⩾20 mm $h^{-1}$) lasted for 5 h (05:00–10:00 on May 11). The first peak in precipitation was at 07:00–08:00 on May 11, when the maximum rainfall

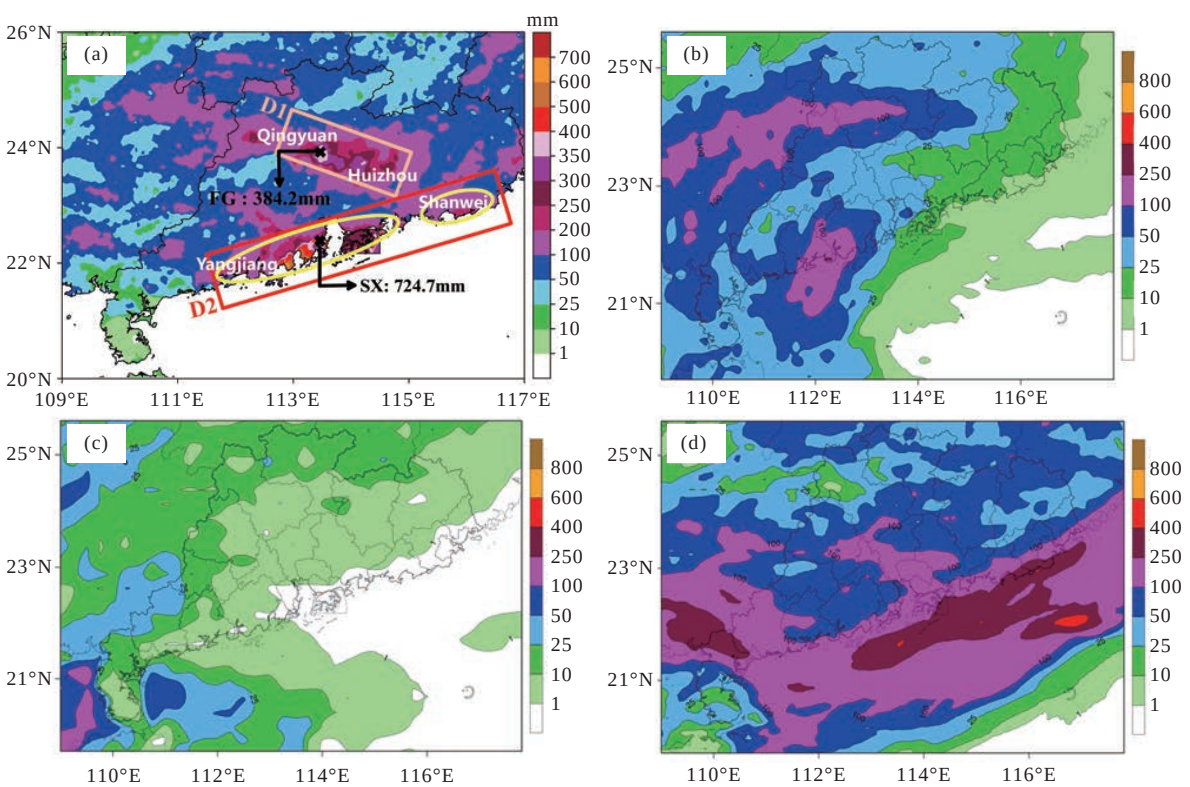


**Figure 2**. (a) The accumulated rainfall from 08:00 BJT May 10 to 08:00 BJT May 13, 2022 (units: mm). D1 represents the northern rain belt, and D2 represents the southern rain belt. "×" denotes the representative site of the double rain belts: Sanxiang (SX) and Fogang (FG). Three-day accumulated rainfall of (b) ECMWF, (c) CMA-GFS, and (d) CMA-GD models forecasted at 08:00 BJT May 10, 2022 (units: mm).

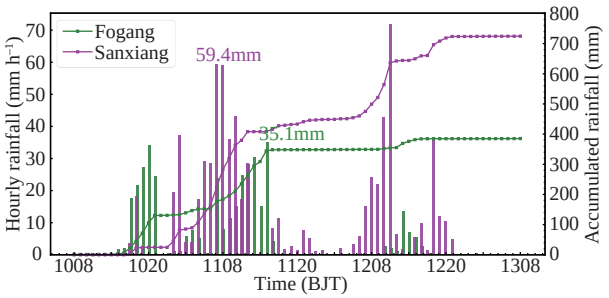


**Figure 3**. The hourly rainfall (bar, units: mm $h^{-1}$) and the accumulated rainfall (fold line, units: mm) from 08:00 BJT May 10 to 08:00 BJT May 13, 2022.

intensity was 59.4 mm $h^{-1}$. The second peak in precipitation was at about 11:00 on May 12, when the maximum rainfall intensity was 71.7 mm $h^{-1}$. The cumulative rainfall increased sharply over a short period and was strongly convectional. The maximum cumulative rainfall of the northern rain belt was 384.2 mm in Fogang. The rainstorm started earlier but was shorter than in the southern rain belt. The precipitation process can be divided into two stages: 15:00–20:00 on May 10 (the rainstorm in the warm sector ahead of the front, accounting for ⩽35% of the cumulative rainfall) and 07:00–16:00 on May 11 (frontal precipitation, accounting for >65%) and the short period of heavy precipitation lasted for 4 h with weak convection. The rainfall intensity was mainly 10–30 mm $h^{-1}$, with a maximum of 35.1 mm $h^{-1}$ at 15:00 on May 11. The precipitation in both rain belts clearly showed different stages. The cumulative rainfall and hourly rainfall intensity in the southern rain belt were both larger, and the convection was stronger than in the northern rain belt.

## 4 ANALYSIS OF THE CAUSE OF THE MESOSCALE RAINSTORM CENTER WITH DOUBLE RAIN BELTS

### 4.1 *Evolution of the mesoscale cloud and rain clusters*

The bright body temperature (TBB) products from the FY2G satellite (Fig. 4) showed that the precipitation in the double rain belts was directly related to $M_\beta$CS-A, $M_\beta$CS-B, and $M_\beta$CS-C, respectively.

The initiation of convection in the southern rain belt was located in the western coastal area. It occurred in the form of scattered convective clouds, resulting in enhanced intensity of precipitation (Fig. 4a). The scattered convective clouds of the southern rain belt initiated and rapidly developed into a massive $M_\beta$CS-A with a horizontal scale of 100–200 km on the western coast. The structure was relatively loose with a TBB ⩽ −62 °C, which led to short-term heavy rainfall at multiple stations, with a local hourly rainfall intensity >50 mm $h^{-1}$ (Fig. 4b). $M_\beta$CS-A organized under highly favorable mesoscale environmental conditions. The area of its cold cloud cover was clearly enlarged, forming an elliptical area of cloud. The gradient of the brightness temperature isoline was asymmetrically distributed, and the brightness temperature on the northern side was significantly decreased (TBB ⩽ −72 °C), indicating that convection had developed to a mature stage. The heavy rainfall was located on the north side of $M_\beta$CS-A, resulting in a local extreme of the hourly rainfall (⩾100 mm $h^{-1}$) (Fig. 4c, d). As $M_\beta$CS-A moved southeast into the sea, the TBB intensity slowly weakened, but the maximum rainfall intensity still exceeded >80 mm $h^{-1}$ (Fig. 4e).

The cloud images show that convective clouds continued to initiate and organize over the northern rain belt. The horizontal scale of $M_\beta$CS-B was about 100 km, with TBB ⩽ −42 °C, resulting in a maximum hourly rainfall intensity >30 mm $h^{-1}$ (Fig. 4f). $M_\beta$CS-C was initiated on the rear side, with a horizontal scale of about 100 km. The intensity of precipitation was further increased, and the maximum rainfall intensity was 44.8 mm $h^{-1}$ (Fig. 4g). $M_\beta$CS-B and $M_\beta$CS-C then merged, and the horizontal scale reached about 200 km, with TBB ⩽ −62 °C maintained in Fogang for a long time with quasi-stationary characteristics. The heavy rainfall was located in the center of $M_\beta$CS-C, and the maximum rainfall intensity was 75.7 mm $h^{-1}$ (Fig. 4h, i). However, the hourly rainfall intensity of $M_\beta$CS-B was generally <10 mm $h^{-1}$. By this time, $M_\beta$CS-A had moved southeast into the sea, so the precipitation range was reduced. The life cycle of $M_\beta$CS-A was as long as 10 h.

This analysis suggests that the double rain belts were caused by isolated mesoscale convective clouds. The rainfall intensity was different between the double rain belts and was closely related to the activity of the mesoscale system. We, therefore, used dual-polarization radar and ground observational data to capture the mesoscale information that favored the occurrence of heavy rain.

### 4.2 *Convective organization and surface mesoscale characteristics of the southern rain belt*

#### 4.2.1 EVOLUTION CHARACTERISTICS OF CONVECTIVE ORGANIZATION IN THE SOUTHERN RAIN BELT

Figure 5 shows that convection in the southern rain belt was initiated with an intensity of 40–45 dBZ in an isolated and scattered manner about 20–30 km from the western coastline. After convection had been initiated, it rapidly developed and strengthened before moving east. The organization was enhanced, and the convection evolved into four banded systems (A, B, C, and D). All the convective systems moved east along the coastline, although the orientation of systems A, B, and D were southwest-northeast, whereas system C was oriented northwest-southeast. Systems A and B merged into a southwest-northeast-oriented linear convective (system E). By contrast, systems C and D evolved into a single massive convection system that grew in size and then organized into a $\beta$ mesoscale convective (system F) with an intensity of 45–55 dBZ. The convective properties were significant, and convective short-term heavy precipitation occurred in the area affected by the echo. System F was highly organized and evolved into a bow-shaped echo, quickly moving southeast. The bow-shaped echo was

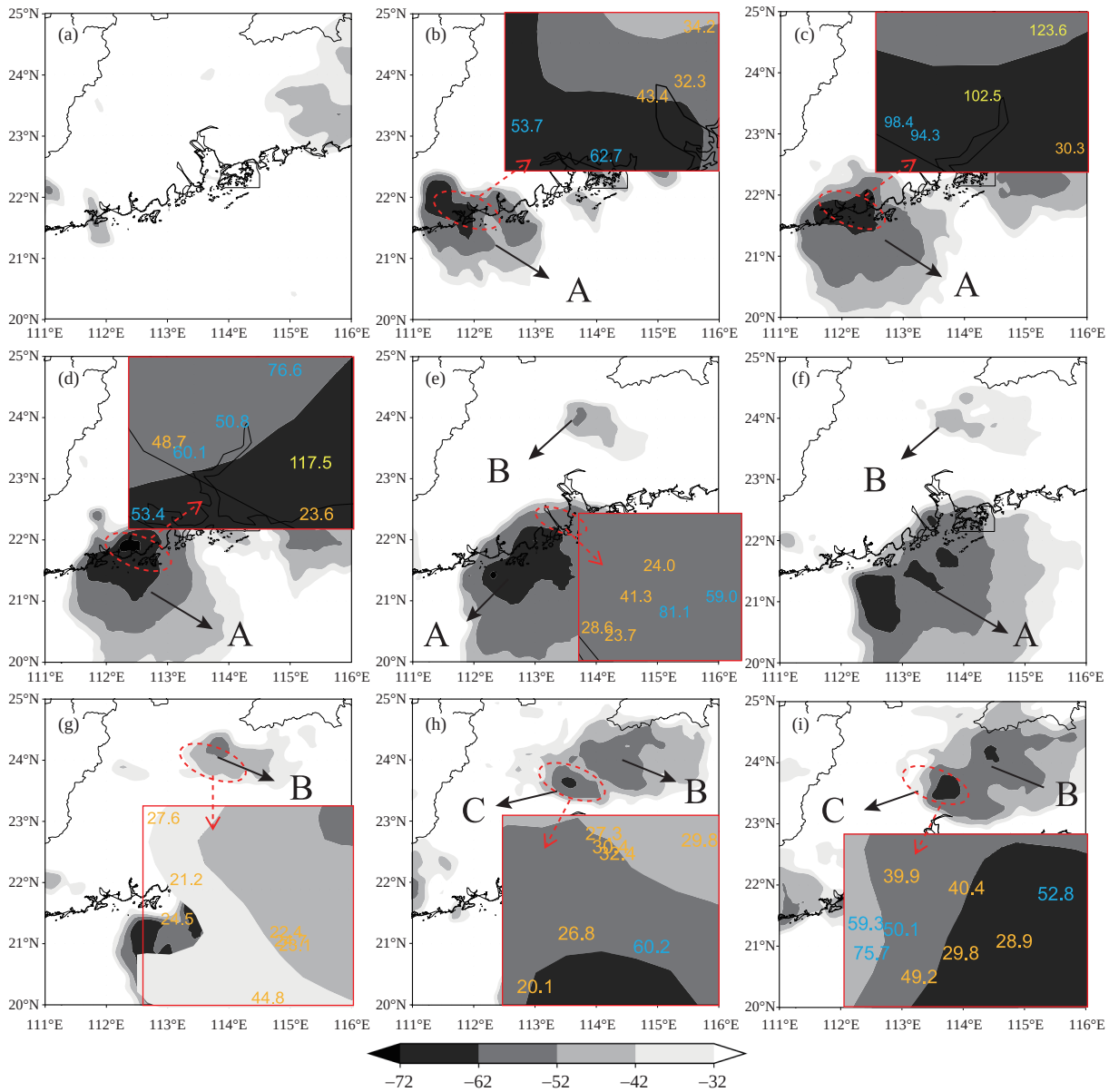


**Figure 4**. Bright body temperature (TBB, units: K) and mesoscale rain clusters at (a) 00:00 BJT, (b) 02:00 BJT, (c) 04:00 BJT, (d) 05:00 BJT, (e) 08:00 BJT, (f) 10:00 BJT, (g) 11:00 BJT, (h) 13:00 BJT, and (i) 14:00 BJT May 11, 2022. The orange, blue, and yellow characters represent the hourly rainfall of 20–49.9 mm $h^{-1}$, 50–99.9 mm $h^{-1}$, and $\geqslant$100 mm $h^{-1}$.

followed by a <40 dBZ stratiform cloud echo, similar to the LS-type linear convective system proposed by Parker et al. [36].

4.2.2 CAUSES OF CONVECTIVE ORGANIZATION IN THE SOUTHERN RAIN BELT

Surface observations (Fig. 6) showed some cold pool centers along the mountains in the west, leading to a temperature difference of about 2°C with the coast. Many studies have confirmed that warm convection in coastal South China is very dependent on the dynamic uplift of the surface cold pool outflow, which leads to the continuous triggering of convection (Wang et al. [37]; Luo and Chen [38]; Wu and Luo [39]). This favors the maintenance of convection intensity and the continuous occurrence of heavy precipitation. The convective cells were isolated and scattered on the western coast and then gradually organized into banded convective systems. This was caused by the interactions between the strengthening southeasterly winds on the ground and the weak northerly winds formed by the cold pool outflow in the western mountainous area. The characteristic bow-shaped echo did not appear at this time.

When the low-level jet had been established, the western coast was located in the export convergence area of the low-level jet, and the warm-moist instability conditions were enhanced. The cold pool formed by the previous precipitation was affected by the low-level jet, which initiated and strengthened convection. The warm-moist air continued to increase on the cold pool, forming a southwest–northeast-oriented cyclonic shear line along the western side of the Zhujiang River estuary. The temperature difference between the two sides of the

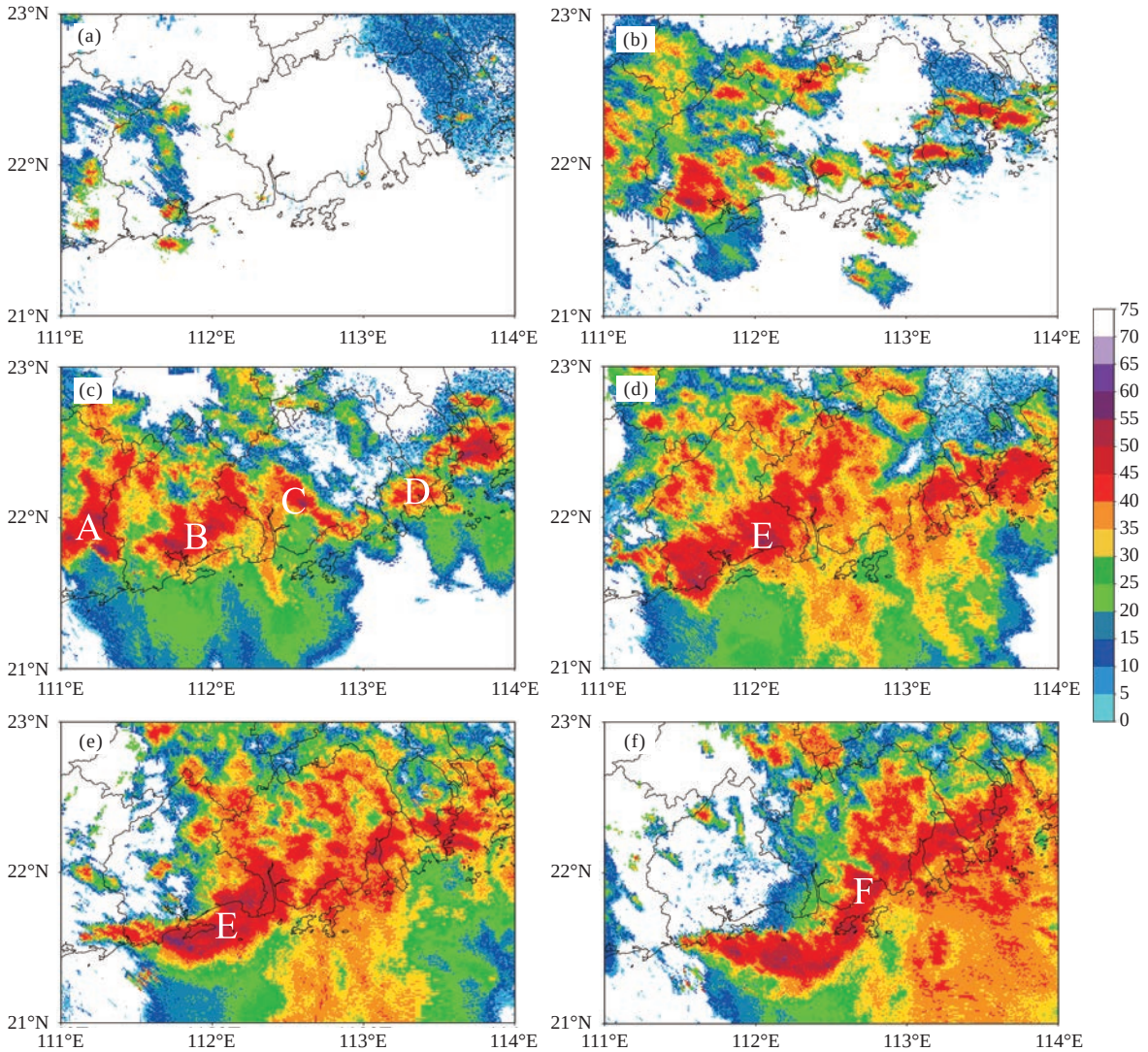


**Figure 5**. Radar reflectivity (units: dBZ) on the west side of Zhujiang River estuary at (a) 22:00 BJT May 10 and (b) 00:00 BJT, (c) 02:00 BJT, (d) 04:00 BJT, (e) 06:00 BJT, and (f) 08:00 BJT May 11, 2022.

cyclonic shear line was about 2 °C. The region south of the cyclonic shear line was a high-energy area with temperatures ⩾25 °C and atmospheric precipitable water ⩾60 mm. This helped to strengthen the convergence of convection and released unstable energy in the high-energy area. Convection continued to develop strongly, resulting in short-term heavy precipitation in many places along the western side of the Zhujiang River estuary. Fig. 5d shows that convection increased rapidly and was highly organized into a $\beta$-mesoscale linear convective system (system E). Several strong convective cells were embedded in the stratiform cloud echo on its eastern side. The linear convective system E merged with these convective cells and moved east along the large-value area of the coastal temperature gradient. As a result of the favorable arc-shaped bay terrain along the Yangjiang coast, the surface winds along the coast showed clear cyclonic convergence at 04:00–06:00, resulting in significant strengthening of the updraft and strong convection. Convective system E gradually evolved into a bow-shaped echo (system F). Previous studies have shown that there are two reasons for a bow-shaped echo. One is closely related to the rear-inflow jet (Smull and Houze [40]; Rotunno et al. [41]; Lafore and Moncrieff [42]; Weisman [43]; Grim et al. [44]; Meng and Zhang [45]) and the other is that the squall line/linear convection merges with the isolated convective cells on its front side (Wolf [46]; Lapenta et al. [47]; French et al. [48]). There was no isolated cell activity in the front of the organized linear convective system in system E, which was clearly not a combined bow-shaped echo. The generation of the bow-shaped echo may, therefore, be related to the rear-inflow jet, which led to extreme heavy rainfall >100 mm $h^{-1}$ in Yangjiang. The northwesterly flow behind the short wavelength trough at 500 hPa rapidly pushed the bow-shaped echo from the land to the ocean. The intensity of precipitation in the southern rain belt, therefore, decreased significantly.

### 4.3 *Convective initiation and mesoscale evolution of the northern rain belt*

The evaporative cooling effect of heavy precipitation

in the northern rain belt on the afternoon of May 10 (Fig. 3) formed a cold pool in the inland mountainous area. The temperature was lower than in the non-precipitation area, and a clear mesoscale boundary (urban heat island and cold pool effect) was formed. The temperature difference on either side of the mesoscale boundary remained at about 2°C.

In the early morning of May 11 (Fig. 7a, b, d, e), the enhanced surface southeasterly warm–humid airflow (about 2 m $s^{-1}$) climbed along the cold pool formed by the earlier precipitation and was forced upward by the small- and medium-scale topography of the key area (about 400 m), triggering convection. The echo intensity of the stratiform cloud rainband was 25–40 dBZ, and the echo intensity of the convective cell in the rain belt was 55–60 dBZ. At this time, the range of influence of the echo was small, but the characteristics of local heavy precipitation were prominent. The echo was significantly strengthened to >40 dBZ at 06:00 on May 11 (Fig. 7c, f), and the range of influence was expanded. The northerly wind formed by the outflow of the cold pool was equivalent to the wind speed of a southeasterly warm-humid airflow (2 m $s^{-1}$), causing confrontation. The northerly wind formed by a shallow cold pool on the northern side was unable to cross the terrain height, resulting in the strong echo center being maintained in a stable state at the boundary between the urban area of Qingyuan and Fogang. Therefore, under a background of strong synoptic-scale forcing, the interaction between the surface-enhanced southeasterly warm-humid airflow, the urban heat island effect, the cold pool formed by the earlier precipitation, and the mesoscale topography all acted together to trigger the initial convection in northern rain belt.

Low-level vortices were generated and developed at 850 and 925 hPa in the northern rain belt. Fig. 8c, d shows that the strong echo stagnated, and the boundary to the south of the echo was flat. The ground observations (Fig.

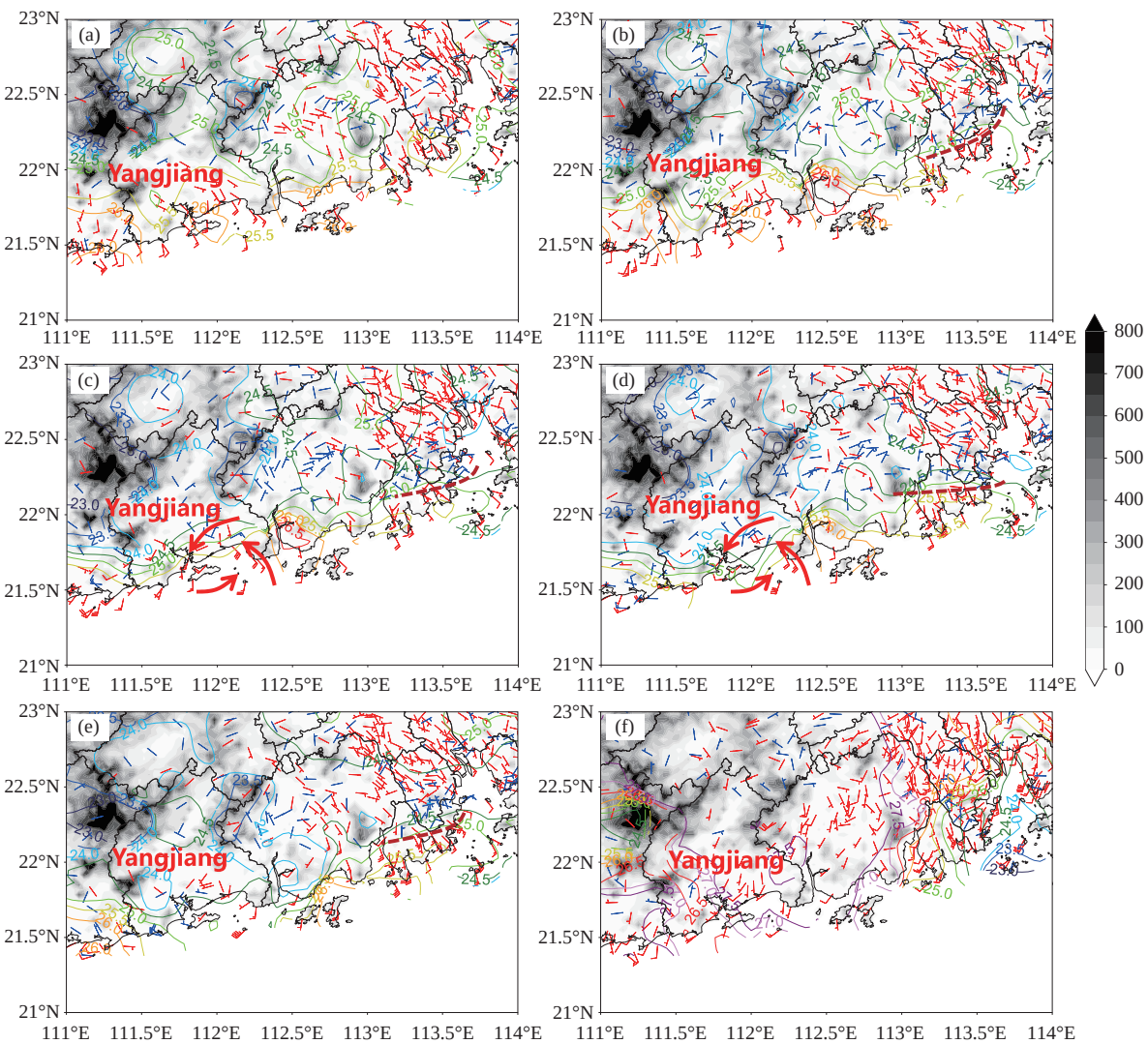


**Figure 6**. Observed surface wind and temperature field (contour lines, units: °C) at (a) 00:00 BJT, (b) 02:00 BJT, (c) 04:00 BJT, (d) 06:00 BJT, (e) 08:00 BJT, and (f) 13:00 BJT May 11, 2022. Wind barbs with a northerly component are in blue, and those with a southerly component are in red (units: m $s^{-1}$); the red curves in (c) and (d) denote cyclonic convergence; brown dotted lines in (c), (d) and (e) denote cyclonic shear line; the grey shading represent terrain (units: m).

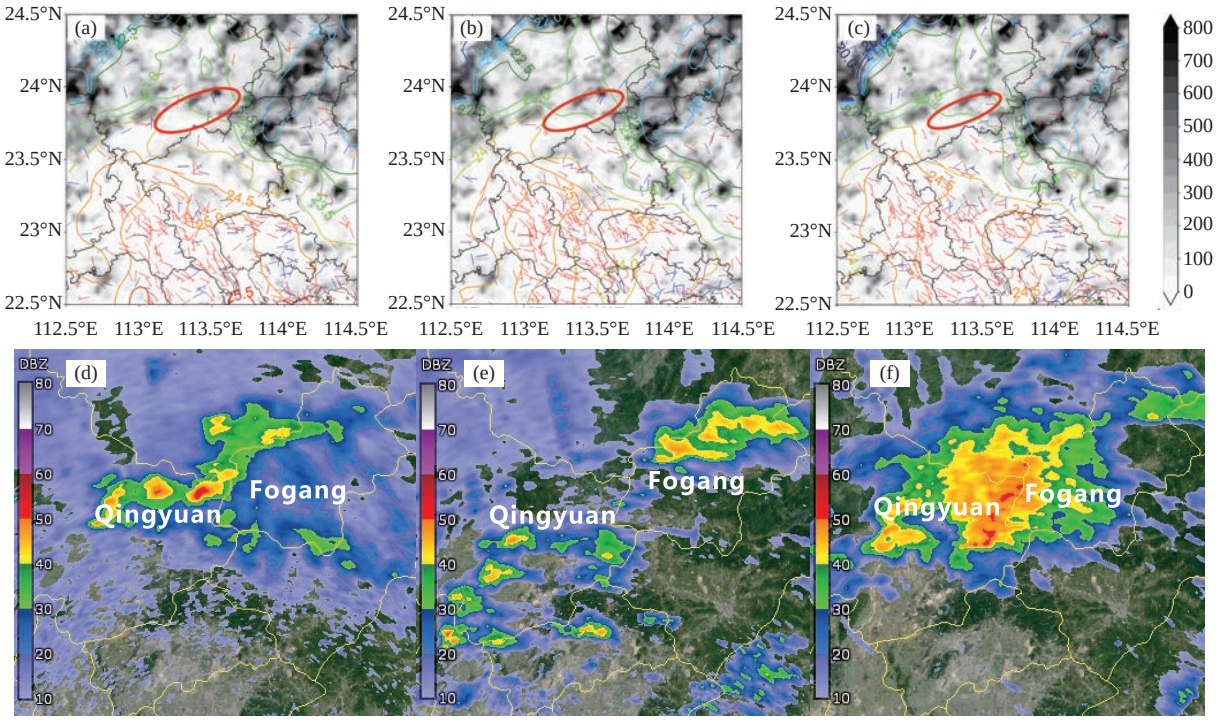


**Figure 7**. As in Fig. 6, and reflectivity at 0.5° elevation from Guangzhou dual-polarization radar at (a, d) 00:00 BJT, (b, e) 04:00 BJT, and (c, f) 06:00 BJT May 11, 2022. The red circles in (a), (b), and (c) represent the key area of the convection triggering.

8a, b) show that the northerly wind formed by the cold pool outflow on the northern side continuously lifted the warm-humid unstable air in front, resulting in new convection being triggered in the leading edge. There was only a small temperature difference (about 2–3°C) between Fogang and the southern side. The north wind formed by the outflow of the cold pool had the same wind speed as the warm-humid airflow in front of the cold pool (about 2 m $s^{-1}$), so there was no obvious outflow wind in front of the cold pool. The warm-humid airflow climbed along the cold wedge formed by the heavy precipitation, and water vapor was fully condensed during the lifting process, resulting in heavy precipitation. At this time, the near-ground cold pool was very shallow. The interaction with the small-scale topography on the southern side of the strong echo (Mt Wangzi, elevation 581.2 m) made the vortex move slowly south due to the small difference between the temperature and wind speed of the cold pool outflow and the warm-humid air. This may be an important reason for the long-term maintenance of the uplift mechanism in which a strong echo can be maintained in a stable state for a long time.

The dragging subsidence and evaporative cooling of heavy precipitation deepened the thickness of the cold pool, which reached 1.5 km (Fig. 8e). The maximum wind speed of the northerly wind formed by the outflow of the cold pool reached about 4 m $s^{-1}$, so the cold pool was able to cross Mt Wangzi. The mesoscale outflow boundary expanded rapidly to the south, guiding the echo to move east and south, and the shape of the echo evolved from a block echo to a linear echo. The maximum of the gate-to-gate difference in the azimuthal radial velocity (over an azimuthal distance of one beamwidth) was >20 m $s^{-1}$ (Fig. 8f), and the distance between the maximum and minimum velocity across the zero line of the radial velocity reached 7–8.5 km, indicating a meso-$\gamma$-scale vortex. This favored the enhancement of convergence and the ascending motion of convection. The maximum rainfall intensity reached 75.7 mm $h^{-1}$. A positive feedback mechanism was, therefore, formed between the meso-$\gamma$-scale vortex and precipitation, which favored the occurrence of heavy rainfall.

A large number of studies have shown the effect on precipitation of maintaining the mesoscale cold pool in the boundary layer (Wang et al. [37]; Xu et al. [49]). The mechanism by which the echo was maintained stably in this rainfall event was similar to the maintaining mechanism of Mt Wangzi on the Guangzhou "5.7" rainstorm in 2017 (Zeng et al. [50]). In the "5.7" rainstorm process, the $\beta$-mesoscale convective system moved slowly and had quasi-stationary characteristics because the speed of the northerly wind of the cold pool outflow was equal to the wind speed of the warm-humid airflow in front of it and the temperature difference between the two sides was small. The first stage of the Guangzhou "5.7" heavy rainstorm occurred near Mt Wangzi, similar to the rainstorms in this study. The Guangzhou "5.7" heavy rainstorm also had similar environmental conditions, such as a southerly warm-humid airflow, mesoscale topographic forced uplift, and a mesoscale boundary. It was an extreme warm sector precipitation event under the background of weak weather-

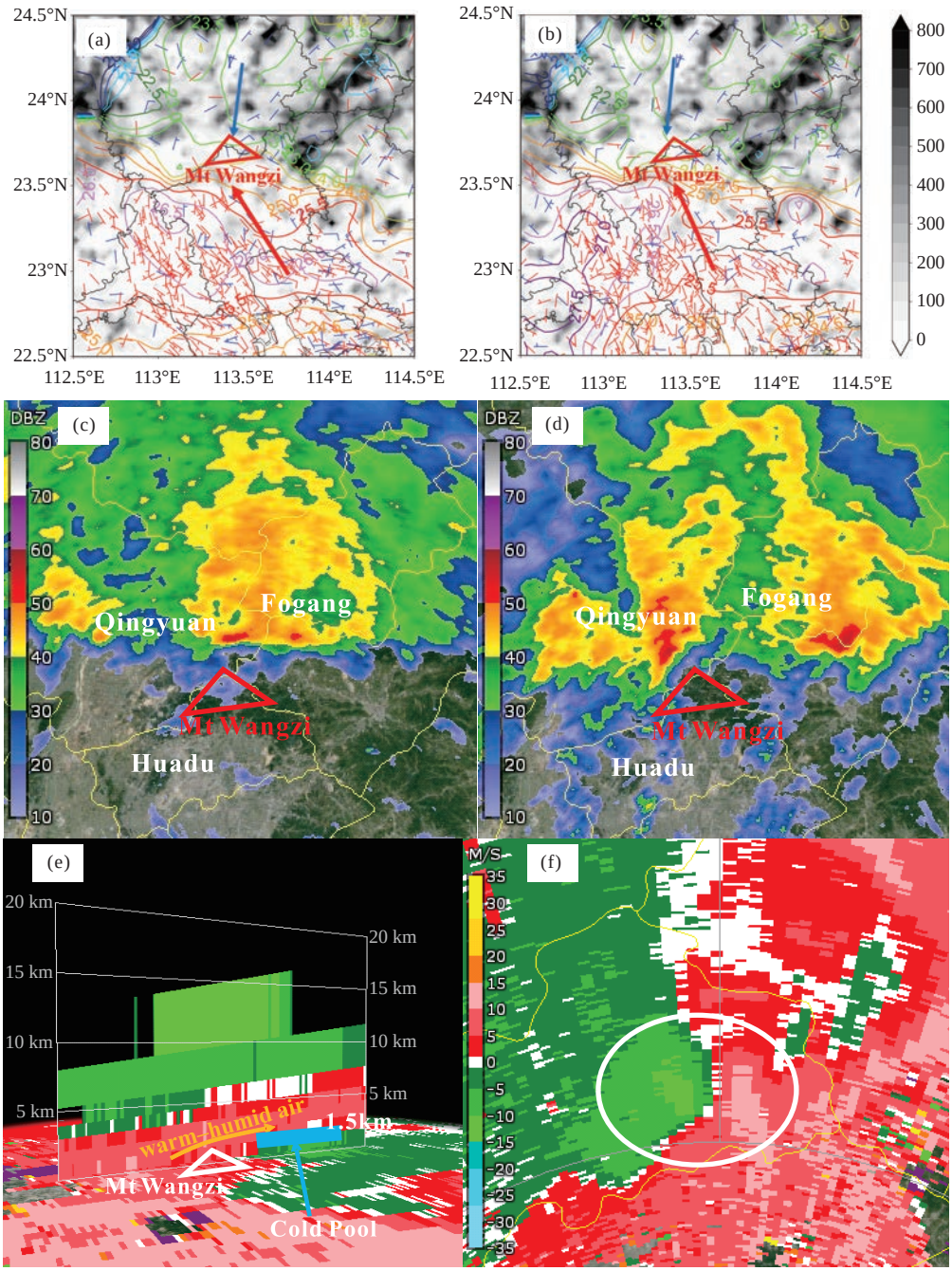


**Figure 8**. Reflectivity at 0.5° elevation from Guangzhou dual-polarization radar and observed surface wind and temperature field at (a, c) 10:00 BJT, and (b, d) 12:00 BJT May 11, 2022. (e) Vertical cross section of radar radial velocity near Mt Wangzi at 12:36 BJT. (f) Radar radial velocity at 13:48 BJT May 11, 2022. The triangles in (a), (b), (c), and (d) denote Mt Wangzi; the white circle in (f) denotes the meso-$\gamma$-scale vortex.

scale forcing. By contrast, the events in our study had a strong weather-scale background with synergistic forcing of the shear line, front, low-level jet, and other systems. We infer from the existing observational data that the topography of Mt. Wangzi could limit the development and southward expansion of the cold pool thickness. As the thickness of the cold pool deepened to 1.5 km and exceeded the altitude of Mt Wangzi, the echo quickly moved south. However, this conclusion requires more data to verify our analysis.

## 5 DIFFERENCES IN CONVECTIVE STRUCTURE AND MICROPHYSICAL CHARACTERISTICS OF THE DOUBLE RAINBAND RAINSTORM CENTER

Since the observation station of the raindrop spectrometer in Zhongshan was far away from the main convective echo area of the southern rain belt, the observation data of the raindrop spectrometer in Zhuhai, which was closest to the rainstorm center of the southern rain belt, can also be used to obtain meaningful conclusions through the direct observation results of the

raindrop spectrometer to a certain extent.

Figure 9 shows the raindrop spectra detected by surface raindrop spectrometers in Zhuhai and Fogang (representing the southern and northern rain belts, respectively). The concentration of small raindrops in the southern rain belt was significantly higher than that of large raindrops during the main precipitation stage of the double rain belts. The raindrop size distribution was wide, and the diameter of most raindrops was >4 mm. By contrast, the number and diameter of the raindrops in the northern rain belt were smaller than in the southern rain belt, and there were fewer raindrops with a diameter >4 mm in most of the periods of precipitation. The number and diameter of raindrops changed synchronously during periods of increased or weakening precipitation in the double rainbands.

To explore the characteristics of the precipitation particles in the double rain belts in more detail, we selected the raindrop spectrum data with similar hourly rainfall intensity in Zhuhai (04:00–05:00) and Fogang (12:00–13:00). Analyses of these raindrop spectra showed that the total number of raindrop particles per hour at these two locations was 78,921 and 80,238, respectively, whereas the total number of particles >2 mm was 3649 and 2815, respectively. The total number of raindrops in both rain belts was therefore comparable, but the hourly rainfall intensity in the southern rain belt was stronger than that in the northern rain belt as a result of the large raindrops.

During the maximum hourly rainfall intensity at Zhuhai (05:00–06:00) and Fogang (14:00–15:00), the total number of raindrop particles was 155,171 and 86,177,

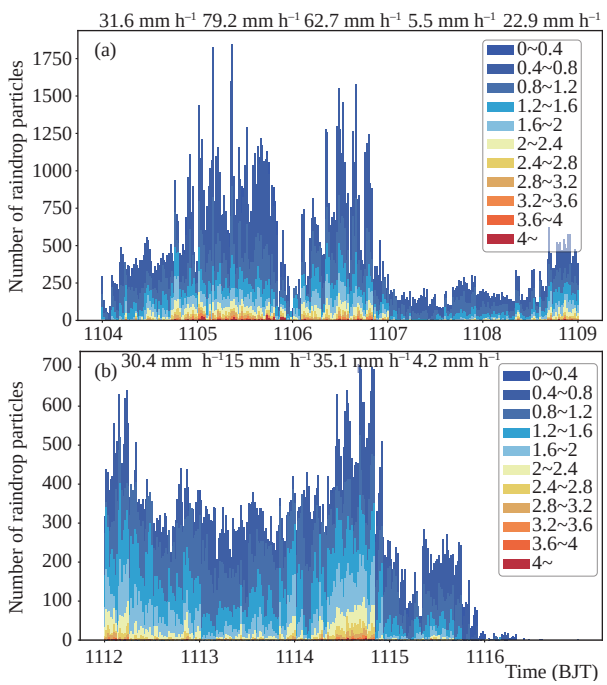


**Figure 9**. The number (bar), diameter (color shading, units: mm), and hourly rainfall hourly rainfall intensity (text label, units: mm $h^{-1}$) detected by surface raindrop spectrometers in (a) Zhuhai from 04:00 BJT to 09:00 BJT May 11, 2022 and (b) Fogang from 12:00 BJT to 16:00 BJT May 11, 2022.

respectively, whereas the total numbers of particles >2 mm were 10,343 and 4058, respectively. The number of small raindrops in the southern rain belt was 2–2.5 times that in the northern rain belt during the period of increasing rainfall intensity. Large particles >2 mm had a longer lifetime in the southern rain belt, and the number of raindrops >3 mm was significantly more than that in the northern rain belt. Based on these analyses, the heavy precipitation in the southern rain belt was caused by the coexistence of both dense large raindrops and small raindrops, whereas the local heavy rainfall in the northern rain belt occurred under the coexistence of relatively dense large and small raindrops.

Dual-polarization radar systems can detect the microphysical characteristics of precipitation particles, such as size, shape, and phase (Zhang et al. [51]; Hu et al. [52]). Fig. 10 shows that the development height of the ⩾50 dBZ strong echo in Sanxiang was about 5.5 km. The 0 °C layer at Yangjiang sounding station is about 5 km. Most of the strong echo was below the 0 °C layer, which had the low centroid echo feature of a tropical ocean. The zero-lag correlation coefficient (CC) of the strong echo region reached >0.95 (the maximum can reach 0.99), indicating that the precipitation particles had the same phase and a similar size. $Z_{DR}$ can be used to distinguish the particle shape of the echo and, combined with other parameters, can be used to judge the size of raindrops (Wang et al. [53]; Song et al. [54]). $Z_{DR}$ was close to 0 dB for ice crystal particles or for <0.3 mm supercooled water droplets above 5.5 km. There was a good match between the area with a large $Z_{DR}$ and the area with a large reflectivity factor–that is, the stronger the reflectivity of the radar echo, the larger the corresponding $Z_{DR}$ value. During the descent process, the $Z_{DR}$ value of the strong echo region increased via a collection process, and the maximum was >2 dB, with the corresponding raindrop particle diameter reaching >2 mm. In general, the particle diameter increased gradually with decreasing height. $K_{DP}$ is closely related to heavy precipitation, and a phase shift of >1 ° $km^{-1}$ is generated by precipitation. The larger the value of $K_{DP}$, the more water droplets are present–that is, the value of $K_{DP}$ reflects the water content. The area with a large $K_{DP}$ value also had a good correspondence with the area with a strong reflectivity factor, reaching 2.5–3° $km^{-1}$. A high density of raindrops, a large particle concentration, and a high liquid water content, therefore, indicate that an area is prone to heavy precipitation, and a change in $K_{DP}$ indicates the occurrence of heavy precipitation.

Figure 11 shows that the radar reflectivity factor at Fogang was clearly weaker than that at Sanxiang, and the convection developed was shallower. Overall, the echo distribution was relatively uniform, and the vertical height of the ⩾40 dBZ echo reached 5.5 km, in which the development height of the local cell was 2 km. The CC of the strong echo area was >0.95, and the maximum reached 0.98. This indicated that the phase and size of the precipitation particles were similar and that their shape

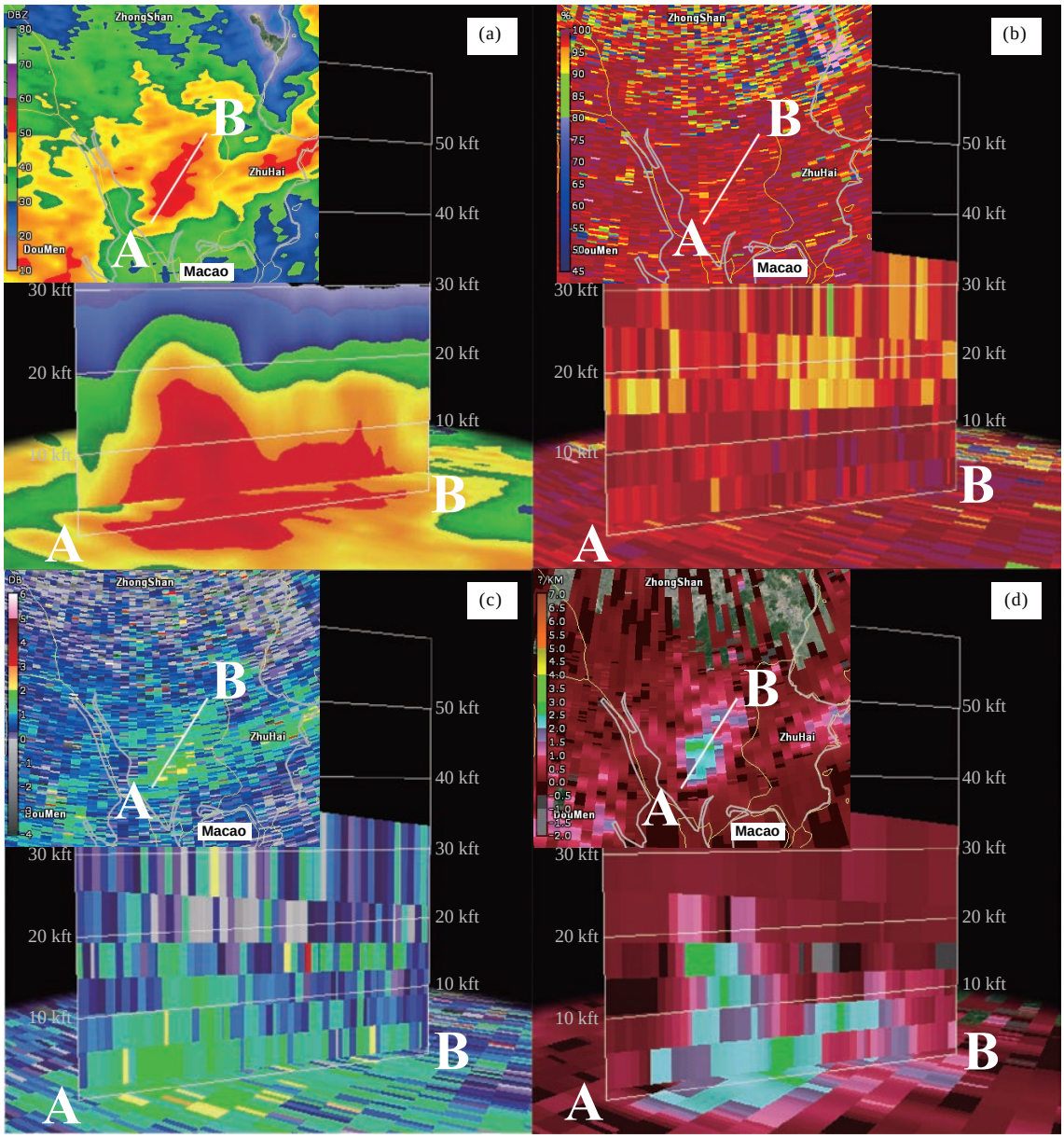


**Figure 10**. Vertical cross sections of (a) radar reflectivity ($Z_H$), (b) zero-lag correlation coefficient (CC), (c) differential reflectivity ($Z_{DR}$), and (d) specific differential phase shift ($K_{DP}$) in Sanxiang at 07:18 BJT May 11, 2022.

and properties were fairly regular. The $Z_{DR}$ value gradually increased during the descent process. The near-surface was dominated by 1.5–2 dB, and the maximum particle diameter was >2 mm. The maximum value of $K_{DP}$ was about 2° km$^{-1}$, so the raindrop density was high.

The results from the raindrop spectrometer and the dual-polarization radar system show that the number and concentration of precipitation particles in the southern rain belt were larger than those in the northern rain belt. There is an error in the diameter of the raindrops in the double rain belts, with the raindrop spectrometer showing that the diameter of raindrops in the southern rain belt was higher than in the northern rain belt. By contrast, the dual-polarization radar results showed that the CC values were similar at the peak time of the hourly rainfall intensity in Sanxiang and Fogang, indicating that the shape and properties of the precipitation particles were relatively uniform. The $Z_{DR}$ values showed that the diameter of the precipitation particles at Fogang was slightly larger than at Sanxiang. Still, the vertical development height of convection at Sanxiang was higher, the intensity was stronger, and there were more raindrops. The convective properties of precipitation and the rainfall intensity were, therefore, stronger in Sanxiang.

The error in the diameter of the precipitation particles may be because, although the raindrop spectrometer in Zhuhai was closer to the rainstorm center in the southern rain belt and was located in the main area of precipitation, it was less accurate at the peak of the hourly rainfall intensity in Sanxiang. In addition, the basic parameters of the dual-polarization radar products (e.g., $Z_{DR}$ and $K_{DP}$) were mainly calculated from the reflection of

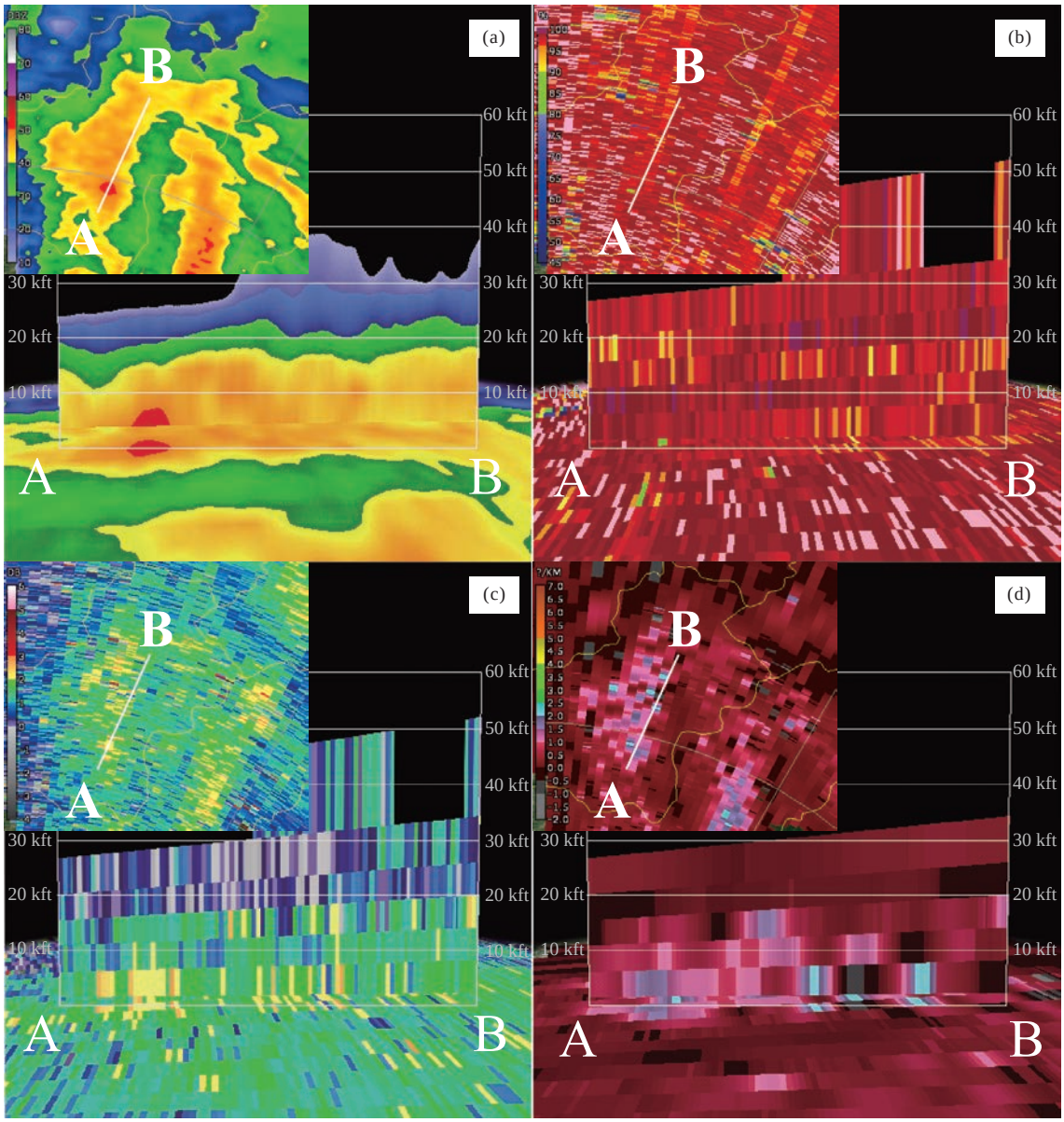


**Figure 11**. As in Fig.10, at 14:36 BJT May 11, 2022 in Fogang.

electromagnetic waves (an indirect observation method), and the dual-polarization radar system was greatly affected by external factors. Based on this analysis, the conclusions obtained from the raindrop spectrometer observations and the dual-polarization parameters were relatively consistent, with only a small error in the raindrop diameter.

## 6 DISCUSSION AND CONCLUSIONS

In this study, a double rain belt event that occurred in South China on May 10–13, 2022, has been investigated by analyzing the atmospheric circulation background atmospheric circulation, characteristics of precipitation, the mesoscale evolution characteristics of the rainstorm centers, and the differences in convective structure and microphysical characteristics of local extreme rainfall. The results can be concluded as follows.

The southern rain belt was formed under weak weather-scale forcing and favorable mesoscale environmental conditions. The northern rain belt was generated under strong weather-scale forcing by a vortex, a low-level shear line, and a frontal system. The rainstorm centers of the double rain belts were generated by isolated mesoscale convective clouds, both of which had clear stages. The accumulated rainfall in the southern rain belt was larger, and the hourly rainfall intensity and convection properties were more significant than in the northern rain belt.

The formation of the southern rain belt was affected by interactions between the enhanced southeasterly wind and the cold pool effect at night, which promoted the continuous development of convection. The cyclonic shear line was formed and maintained as a result of the combined influence of the northerly wind formed by the cold pool outflow and southerly warm-humid air. The strong echo propagated east along the large-value area of the coastal temperature gradient, resulting in continuous heavy rainfall along the western coast of the Zhujiang

River estuary. The surface cyclonic convergence wind field along the western coast enhanced the updraft and the strong development of convection intensity. The existence of a rear-inflow jet may be the main reason for the bow-shaped echo, which led to local extreme rainfall.

In the northern rain belt, the initial convection was triggered by the interaction between the enhanced southeasterly warm–humid airflow at night, the cold pool formed by earlier precipitation, the mesoscale terrain, and the mesoscale boundary. The strong echo in Fogang was stable because the temperature and wind speed difference between the cold pool outflow and warm-humid air on the front side was small. Mt Wangzi had a limited effect on the development and southward expansion of the cold pool thickness. The mesoscale outflow boundary in front of the cold pool expanded southward as the cold pool thickened. The meso-$\gamma$-scale vortex, formed during the rapid eastward and southward movement of the strong echo, enhanced convergence and the upward movement of convection. This formed a positive feedback mechanism with precipitation, which favored the occurrence of heavy rainfall.

The convective structure and microphysical characteristics of the rainstorm center of the double rain belt showed that the radar reflectivity factor was stronger at Sanxiang, the vertical development of convection was slightly higher, and it had the low centroid feature of a tropical ocean. The observations from the raindrop spectrometer showed that the number and concentration of heavy raindrops and small raindrops in the southern rain belt were higher than in the northern rain belt. When the hourly rainfall intensity was almost the same, the larger diameter raindrops in the southern rain belt led to a stronger rainfall intensity even if the total number of raindrops in both rain belts was comparable. The diameter of the raindrops and the number of small raindrops may, therefore, be the cause of the large difference in rainfall intensity between Sanxiang and Fogang.

This paper is only a brief analysis of the double rain belts that occurred in South China on May 10–13, 2022, but it is unique. The numerical model had poor predictability for the development of the low vortex and lacked the ability to describe the occurrence of local heavy precipitation. Under different circulation scenarios, the interaction between the initiation of convection and the cold pool, the mesoscale terrain, and other factors is still difficult to predict. In addition, the mechanism of the surface cyclonic convergence wind field and the bow-shaped echo is unclear during extreme heavy precipitation. An artificial intelligence algorithm could be introduced into short-term nowcasting systems to strengthen short-term monitoring and forecasting in future operational forecasts. This may help to solve the lack of forecasting ability for sudden extreme precipitation events in numerical models. Whether the conclusions in this paper are universal requires research and in-depth comparisons of the formation mechanism and interrelationships with other factors.

## REFERENCES


[1] LIN Que-lue, ZHAO Hua-sheng, LIN Bao-ting. Comparative analysis on backflow warm-sector rainstorm cases in double rain belts process [J]. Journal of Tropical Meteorology, 2020, 36(6): 721–733, https://doi.org/10.16032/j.issn.1004–4965.202–10.065, in Chinese with English abstract

[2] LIN Xiao-xia, FENG Ye-rong, ZHANG Cheng-zhong, et al. Diagnostic analysis of thermal and dynamic characteristics of a rainstorm process in Southern China [J]. Journal of Tropical Meteorology, 2017, 33(6): 975–984, https://doi.org/10.16032/j.issn.1004–4965.2017.06.018, in Chinese with English abstract

[3] ZHANG Xiao-hui, NI Yun-qi. A comparative study of a frontal and a non-frontal convective systems [J]. Acta Meteorologica Sinica, 2009, 67(1): 108–121, in Chinese with English abstract

[4] HALLEGATTE S, GREEN C, NICHOLLS R J, et al. Future flood losses in major coastal cities [J]. Nature Climate Change, 2013, 3(9): 802, https://doi.org/10.1038/nclimate1979

[5] DING Zhi-ying, CHANG Yue, ZHU Li, et al. Research on the reason of the double rain-bands' forming in a sustaining storm rainfall of South China [J]. Journal of Tropical Meteorology, 2008, 24(2): 117–126, in Chinese with English abstract

[6] DING Zhi-ying, ZHU Li, CHANG Yue, et al. Research on the causes of double rain belts during a sustained rainstorm [J]. Journal of Tropical Meteorology, 2009, 25 (6): 698–705, in Chinese with English abstract

[7] DING Zhi-ying, WANG Shuang, GAO Song. Potential vorticity evolution of a double rainbands storm in South China and interactions between the rainbands [J]. Transactions of Atmospheric Sciences, 2017, 40(5): 653–662, https://doi.org/10.13878/j.cnki.dqkxxb.20151226002, in Chinese with English abstract

[8] LIU Xi, LUO Ya-li, HUANG Ling, et al. Roles of double low-level jets in the generation of coexisting inland and coastal heavy rainfall over south China during the pre-summer rainy season [J]. Journal of Geophysical Research: Atmospheres, 2020, 125(18): e2020JD032890, https://doi.org/10.1029/2020JD032890

[9] WANG Hua, LI Hong-yu, ZHONG Ji-qin, et al. The formation of an unusual two-belt heavy rainfall around Beijing-Tianjin-Hebei area [J]. Plateau Meteorology, 2019, 38(4): 856–871, https://doi.org/10.7522/j.issn.1000–0534.2018.00102, in Chinese with English abstract

[10] DU Xiao-ling. Mesoscale ambient field analysis of torrential rains and the forecast key points in Guizhou in 2012 [J]. Meteorological Monthly, 2013, 39(7): 861–873, https://doi.org/10.7519/j.issn.1000–0526.2013.07.007, in Chinese with English abstract

[11] LUO Juan, FENG Jia-xiong, CHEN Mu-xi. Mechanism of two β scale rain belts in the MCS [J]. Journal of Arid Meteorology, 2018, 36(3): 456–464, https://doi.org/11755/j.issn.1006–7639(2018)-03–0456, in Chinese with English abstract

[12] YANG Qing, YAN Qi, CHEN Li-qiang, et al. Analysis of a typical rainstorm with double rain belts in Liaoning province [J]. Journal of Meteorology and Environment, 2015, 31(6): 34–42, https://doi.org/10.3969/j.issn.1673–

503X.2015.06.005, in Chinese with English abstract
[13] YAN Jun-yue, TANG Zhi-yi, YAO Hua-dong, et al. A synoptic study on establishment of the Monsoon and associated variation of rain belt over the South China Sea in 2002 [J]. Acta Meteorologica Sinica, 2003, 61(5): 569–579, in Chinese with English abstract
[14] ZHAO Yu-chun, LI Ze-chun, XIAO Zi-niu. Comparison analysis of South China front and warm-area heavy rain systems in June 2006 [J]. Meteorological Science and Technology, 2008, 36(1): 47–54, https://doi.org/10.19517/j.1671–6345.2008.01.011, in Chinese with English abstract
[15] WANG Shuang. Research on the Formation Mechanism of Different Types Warm Area Heavy Rainfall in Southern China [D]. Nanjing: Nanjing University of Information Science and Technology, 2013, in Chinese with English abstract
[16] ZHAO Si-xiong, ZHOU Xiao-ping. The effect of wind field disturbances on the forecast of rainstorm formation [J]. Chinese Journal of Atmospheric Sciences, 1984, 8(1): 1–6, in Chinese with English abstract
[17] MENARD R D, FRITSCH J M. A mesoscale convective complex-generated inertially stable warm core cortex [J]. Monthly Weather Review, 1989, 117(6): 1237–1261, https://doi.org/ 10.1175/1520–0493(1989)117<1237:AMCCGI>2.0.CO
[18] HUANG Shi-song, LI Zhen-guang, BAO Cheng-lan, et al. Precipitation During the Pre-flood Season in South China [M]. Guangdong: Guangdong Science & Technology Press, 1986: 94–95, in Chinese with English abstract
[19] BAO Cheng-lan. Advances of rainstorm in pre-flood season in South China [J]. Acta Oceanologica Sinica, 1986, 8(1): 31–40, in Chinese with English abstract
[20] XIA Ru-di, ZHAO Si-xiong. Diagnosis and modeling of meso-β-scale systems of heavy rainfall in warm sector ahead of front in South China (middle part of Guangdong Province) in June 2005 [J]. Chinese Journal of Atmospheric Sciences, 2009, 33(3): 468–488, in Chinese with English abstract
[21] MIAO Chun-sheng, YANG Yi-ya, WANG Jian-hong, et al. Comparative study of characteristics and thermodynamical development mechanism on two types of warmsector heavy rainfall in South China coast [J]. Journal of Tropical Meteorology, 2017, 33(1): 53–63, https://doi.org/10.16032/j.issn.1004–4965.2017.01.006, in Chinese with English abstract
[22] LI Bo, LIU Li-ping, ZHAO Si-xiong, et al. Numerical experiment of the effect of local terrain on heavy rainstorm of South China [J]. Plateau Meteorology, 2013, 32(6): 1638–1650, https://doi.org/10.7522/j.issn.1000–0534.2012.00156, in Chinese with English abstract
[23] WANG Jian-hong, YANG Yi-ya, MIAO Chun-sheng, et al. The numerical study of terrain dynamic influence on warm area heavy rainfall of convergence lines in South China coast [J]. Chinese Journal of Atmospheric Sciences, 2017, 41(4): 784–796, https://doi.org/10.3878/j.issn.1006–9895.1702.16182, in Chinese with English abstract
[24] KONG Qi, LIN Jian. Analysis on causes and forecasts of the torrential rainfall with different features over South China during 19 to 20 May 2015 [J]. Meteorological Monthly, 2017, 43(7): 792–803, https://doi.org/10.7519/j.issn.1000–0526.2017.07.003, in Chinese with English abstract
[25] MENG Wei-guang, WANG An-yu, LI Jiang-nan, et al. Multi-MCSs (mesoscale convective systems) over the heavy rainfall region during 23–24 May 1998 in South China [J]. Acta Scientiarum Naturalium Universitatis Sunyatseni, 2003, 3: 73–77, in Chinese with English abstract
[26] ZHANG Xiao-mei, MENG Wei-guang, ZHANG Yan-xia, et al. Analysis of mesoscale convective systems associated with a warm sector heavy rainfall event over South China [J]. Journal of Tropical Meteorology, 2009, 25(5): 551–560, https://doi.org/10.3969/j.issn.1004–4965.2009.05.005, in Chinese with English abstract
[27] SUN Ji-song, LEI lei, YU Bo, et al. The fundamental features of the extreme severe rain events in the recent 10 years in the Beijing area [J]. Acta Meteorologica Sinica, 2015, 73(4): 609–623, https://doi.org/10.11676/qxxb2015.044, in Chinese with English abstract
[28] YANG Chun, CHEN Yun, FANG Zhi-fang, et al. Multi-scale characteristics analysis of Liuzhou server rainfall in June, 2007 [J]. Meteorological Monthly, 2009, 35(6): 54–62, in Chinese with English abstract
[29] HE Song-wei, GAO Jian-qiu, ZHONG Jian-hong, et al. Analysis of microphysical characteristics of springtime precipitation in northern Guangdong Province [J]. Guangdong Meteorology, 2022, 44(3): 6–10, in Chinese with English abstract
[30] YE Lang-ming, XU Bi-yu, LIU Xian-tong, et al. Maintenance mechanism and microphysical characteristics of an extreme intensity precipitation in warm area in western Guangdong in 2017 [J]. Climatic and Environmental Research, 2021, 26(3): 263–274, https://doi.org/10.3878/j.issn.1006–9585.2020.20028, in Chinese with English abstract
[31] HAN Bin, DU Yu, WU Chong, et al. Microphysical characteristics of the coexisting frontal and warm-sector heavy rainfall in South China [J]. Journal of Geophysical Research: Atmospheres, 2021, 126(21): e2021JD035446, https://doi.org/10.1029/2021JD035446
[32] CHEN Yun, CHEN Tao, WANG Ling-yao, et al. A review of the warm-sector rainstorms in China [J]. Torrential Rain and Disasters, 2019, 38(5): 483–493, https://doi.org/10.3969/j.issn.1004–9045.2019.05.010, in Chinese with English abstract
[33] WU Nai-geng, WEN Zhi-ping, DENG Wen-jian, et al. Advances in warm-sector heavy rainfall during the first rainy season in South China [J]. Journal of the Meteorological Sciences, 2020, 40(5): 605–616, https://doi.org/10.3969/2020jms.0077, in Chinese with English abstract
[34] WU Meng-wen, LUO Ya-li. Mesoscale observational analysis of lifting mechanism of a warm-sector convective system producing the maximal daily precipitation in China mainland during pre-summer rainy season of 2015 [J]. Journal of Meteorological Research, 2016, 30(5): 719–736, https://doi.org/10.1007/s13351–016–6089–8
[35] HE Li-fu, CHEN Tao, KONG Qi. A review of studies on prefrontal torrential rain in South China [J]. Journal of Applied Meteorological Science, 2016, 27(5): 559–569, https://doi.org/10.11898/1001–7313.20160505, in Chinese with English abstract
[36] PARKER M D, JOHNSON R H. Organizational modes of

midlatitude mesoscale convective systems [J]. Monthly Weather Review, 2000, 128(10): 3413–3436, https://doi.org/10.1175/1520–0493(2001)129<3413:OMOMMC>2.0.CO;2

[37] WANG Hui, LUO Ya-li, JOU B J D. Initiation, maintenance, and properties of convection in an extreme rainfall event during SCMREX: Observational analysis [J]. Journal of Geophysical Research: Atmospheres, 2014, 119(23): 13206–13232, https://doi.org/10.1002/2014JD022339

[38] LUO Ya-li, CHEN Yang-ruixue, Investigation of the predictability and physical mechanisms of an extreme-rainfall-producing mesoscale convective system along the Meiyu front in East China: An ensemble approach [J]. Journal of Geophysical Research: Atmospheres, 2015, 120 (20): 10593–10618, https://doi.org/10.1002/2015JD023584

[39] WU Meng-wen, LUO Ya-li. Mesoscale observational analysis of lifting mechanism of a warm-sector convective system producing the maximal daily precipitation in China mainland during pre-summer rainy season of 2015 [J]. Journal of Meteorological Research, 2016, 30(5): 719–736, https://doi.org/10.1007/s13351–016–6089–8

[40] SMULL B F, HOUZE R A. A midlatitude squall line with a trailing region of stratiform rain: Radar and satellite observations [J]. Monthly Weather Review, 1985, 113(1): 117–133, https://doi.org/10.1175/1520–0493(1985)113<0117:AMSLWA>2.0.CO;2

[41] ROTUNNO R, KLEMP J B, WEISMAN M L. A theory for strong, long-lived squall lines [J]. Journal of the Atmospheric Sciences, 1988, 45(3): 463–485, https://doi.org/10.1175/1520–0469(1988)045<0463:ATFSLL>2.0.CO;2

[42] LAFORE J P, MONCRIEFF M W. A numerical investigation of the organization and interaction of the convective and stratiform regions of tropical squall lines [J]. Journal of the Atmospheric Sciences, 1989, 46(4): 521–544, https://doi.org/10.1175/1520–0469(1989)046<0521:ANIOTO>2.0.CO;2

[43] WEISMAN M L. The role of convectively generated rear-inflow jets in the evolution of long-lived mesoconvective systems [J]. Journal of the Atmospheric Sciences, 1992, 49 (19): 1826–1847, https://doi.org/10.1175/1520–0469(1992)049<1826:TROCGR>2.0.CO;2

[44] GRIM J A, RAUBER R M, MCFARQUHAR G M, et al. Development and forcing of the rear inflow jet in a rapidly developing and decaying squall line during BAMEX [J]. Monthly Weather Review, 2009, 137(4): 1206–1229, https://doi.org/10.1175/2008mwr2503.1

[45] MENG Zhi-yong, ZHANG Fu-qing, MARKOWSKI P, et al. A modeling study on the development of a bowing structure and associated rear inflow within a squall line over South China [J]. Journal of the Atmospheric Sciences, 2012, 69(4): 1182–1207, https://doi.org/10.1175/jas-d-11–0121.1

[46] WOLF P L. WSR-88D radar depiction of supercell-bow echo interaction: Unexpected evolution of a large, tornadic, “comma-shaped” supercell over eastern Oklahoma [J]. Weather and Forecasting, 1998, 13(2): 492–504, https://doi.org/10.1175/1520–0434(1998)013<0492:WRDOSB>2.0.CO;2

[47] LAPENTA K D, BOSART L F, GALARNEAU T J, et al. A multiscale examination of the 31 May 1998 Mechanicville, New York, tornado [J]. Weather and Forecasting, 2005, 20 (4): 494–516, https://doi.org/10.1175/WAF875.1

[48] FRENCH A J, PARKER M D. Observations of mergers between squall lines and isolated supercell thunderstorms [J]. Weather and Forecasting, 2012, 27(2): 255–278, https://doi.org/10.1175/waf-d-11–00058.1

[49] XU Wei-xin, ZIPSER E J, CHEN Yi-leng, et al. An orography-associated extreme rainfall event during TiMREX: initiation, storm evolution, and maintenance [J]. Monthly Weather Review, 2012, 140(8): 2555–2574, https://doi.org/ 10.1175/MWR-D-11–00208.1

[50] ZENG Zhi-lin, CHEN Yun, ZHU Ke-yun, et al. Mesoscale characteristic analysis and primary discussion on the formation of the 7 May 2017 torrential rainfall in Guangzhou [J]. Journal of Tropical Meteorology, 2018, 34 (6): 791–805, https://doi.org/10.16032/j.issn.1004–4965.2018.06.008, in Chinese with English abstract

[51] ZHANG Yu, HU Dong-ming, LI Huai-yu. Preliminary application of a dual polarization weather radar in Guangzhou during a short- range intensive rain [J]. Guangdong Meteorology, 2017, 39(2): 26–29, https://doi.org/10.3969/j.issn.1007–6190.2017.02.006, in Chinese with English abstract

[52] HU Ya-jun, ZHANG Wei, ZHAO Yu-chun, et al. Mesoscale feature analysis on a warm-sector torrential rain event in southeastern coast of Fujian on 7 May 2018 [J]. Meteorological Monthly, 2020, 46(5): 629–642, https://doi.org/10.7519/j.issn.1000–0526.2020.05.004, in Chinese with English abstract

[53] WANG Kun, WANG Xiao-hua, XIA Xin, et al. Microphysical characteristics of the extremely heavy rainstorm observed by Jiangsu polarimetric radars network in southeastern Jiangsu on July 17, 2019 [J]. Journal of the Meteorological Sciences, 2022, 42(5): 610–621, https://doi.org/10.12306/2022jms.0050, in Chinese with English abstract

[54] SONG Wen-ting, LI Yun-ying, HUANG Hao, et al. Hydrometeors classification and its application based on S-band dual polarization radar data [J]. Transactions of Atmospheric Sciences, 2021, 44(2): 209–218, https://doi.org/10.13878/j.cnki.dqkxxb.20200318001, in Chinese with English abstract

**Citation:** GUO Zhao-hua, CHEN Yun, XIAO Tian-gui, et al. Mesoscale and Microphysical Characteristics of a Double Rain Belt Event in South China on May 10–13, 2022 [J]. Journal of Tropical Meteorology, 2024, 30(1): 61-75, https://doi.org/10.3724/j.1006-8775.2024.007